A Novel GNSS Single-Frequency PPP Approach to Estimate the Ionospheric TEC and Satellite Pseudorange Observable-Specific Signal Bias

Ke Su and Shuanggen Jin, *Senior Member, IEEE*

***Abstract*— As the significant error sources influencing the Global Navigation Satellite System (GNSS) positioning, navigation, and timing (PNT) services, ionospheric delay and satellite hardware delay should be properly calibrated. Particularly, the pseudorange observable-specific signal bias (OSB) is convenient and can be directly corrected in the raw pseudorange measurement. In this work, we present a novel single-frequency ionospheric-free-half precise point positioning (PPP) (SFPPP2) approach for ionospheric studies, in which the ionospheric vertical total electron content (VTEC) and satellite OSB are isolated from the slant ionospheric observables by means of the ionospheric multilayer mapping function (MF). The computation and parameterization methods of the ionospheric VTEC and satellite pseudorange OSB are present. To validate the effectiveness and reliability of the novel method, we investigate and compare the performance of the single-frequency ionospheric-float PPP (SFPPP1), SFPPP2, and dual-frequency ionospheric-float PPP (DFPPP1) solutions for ionosphere sensing. The analytical results indicate that the novel approach can extract the slant ionospheric observables with the accuracy of submeters. The accuracy of the estimated ionospheric VTEC by the single-frequency PPP approaches is in the submeter level, which exhibits a slightly worse accuracy than that from the dual-frequency PPP solution. The estimated ionospheric VTEC accuracy is improved with the multilayer MF compared with the single-layer MF. The estimated BeiDou Navigation Satellite System (BDS) pseudorange OSB with the proposed SFPPP2 approach is stable, reliable, and of the high accuracy, and the rms's with respect to Chinese Academy of Sciences (CAS) product for C2I and C6I signals with single-layer and multilayer MFs are 0.40, 0.41, 0.60, and 0.63 ns, respectively. The proposed PPP approach can retrieve the VTEC and satellite pseudorange OSB by mass-market receivers for the GNSS users.**

***Index Terms*— Multilayer mapping function (MF), observable-specific signal bias (OSB), single-frequency precise point positioning (PPP), vertical total electron content (VTEC).**

I. Introduction

With the resounding success of the Global Navigation Satellite System (GNSS) development, more than 100 navigation satellites transmitting multiple frequencies with various modulations are on-orbit now. The newly established Beidou Navigation Satellite System (BDS) and Galileo systems, as well as the global positioning system (GPS) and GLONASS, have experienced dramatic developments [1]–[3]. The integration of the multiple frequencies has become the GNSS developing trend, which brings about more opportunities and challenges for ionosphere sensing and other GNSS applications [4], [5]. The ionospheric regional and global spatiotemporal characteristics can be investigated by GNSS measurements due to their continuous observing features. The multi-GNSS integration enables more viable satellites and, thus, increases the ionospheric pierce point (IPP) distributing density [6]. The GNSS-based ionosphere sensing has the advantages of global coverage, high precision, all-weather availability, and so on, which has been investigated for numerous years [7], [8].

Ionospheric and hardware delays are the significant error sources in the GNSS measurements. Single-frequency GNSS users need the extra correction on account of the ionospheric delay errors whose magnitude is tens of meters, in which the precise positioning performance is directly affected. The satellite differential code bias (DCB) is defined as the satellite pseudorange hardware delay between the signals of different tracking channels and frequencies, which is affected by the factors of the temperature, hardware conditions, and so on [9]. The extracted ionospheric observables are usually coupled with DCB due to the ionosphere dispersive characteristic. The satellite DCB values, estimated in conjunction with the ionosphere modeling or using the external prior ionosphere information from the multifrequency GNSS measurements, are routinely provided as the daily multi-GNSS DCB products from the Chinese Academy of Sciences (CAS) and the German Aerospace Center (DLR) [10], [11]. In fact, the DCB corrections are relatively complex and inconvenient to be adapted to the multi-GNSS and multifrequency scenarios. The effective alternative method is to parametrize the pseudorange bias in the undifferenced forms. The concept of the pseudorange observable-specific signal bias (OSB) is defined in both standard of the Radio Technical Commission for Maritime Service and SINEX format 1.00 [12], [13]. The OSB is more straightforward and can be directly corrected in the raw measurement. The daily multi-GNSS OSB products have been provided by the Center for Orbit Determination in Europe (CODE) and CAS [14], [15].

Manuscript received June 15, 2021; revised July 30, 2021, September 11, 2021, and October 29, 2021; accepted November 2, 2021. Date of publication November 8, 2021; date of current version February 15, 2022. This work was supported in part by the National Natural Science Foundation of China Project under Grant 12073012 and in part by the National Natural Science Foundation of China-German Science Foundation Project under Grant 41761134092. *(Corresponding author: Shuanggen Jin.)*

Ke Su is with the Shanghai Astronomical Observatory, Chinese Academy of Sciences, Shanghai 200030, China, and also with the School of Astronomy and Space Science, University of Chinese Academy of Sciences, Beijing 100049, China (e-mail: ksu@shao.ac.cn).

Shuanggen Jin is with the Shanghai Astronomical Observatory, Chinese Academy of Sciences, Shanghai 200030, China (e-mail: sgjin@shao.ac.cn).

Digital Object Identifier 10.1109/TGRS.2021.3126397

Generally, the carrier-to-code leveling (CCL) and precise point positioning (PPP) are the two commonly used methods to extract the arc-by-arc slant ionospheric observables encompassing the total electron content (TEC), as well as the receiver and satellite hardware delays [16], [17]. In the CCL technique, the absolute but noisy observables are aligned by the ambiguous but precise carrier phase observables using arc-by-arc dual-frequency measurements, and then, the slant ionospheric observables are yielded. With sufficient available observations, the pseudorange noise effect will significantly decrease. However, the leveling errors arising from the multipath effect still evidently exist and cannot be eliminated in the CCL method. With respect to the PPP, the dual-frequency or multifrequency approaches are currently the state of the art to sense the ionosphere with the external precise satellite orbit and clock products. For instance, Shi *et al.* [18] estimated the slant ionospheric observables and satellite DCB by the dual-frequency ionosphere-float PPP (DFPPP1) and CCL methods. Chen *et al.* [19] evaluated the accuracy, difference, and usability of the slant ionospheric observables extracted from the CCL, DFPPP1, and UofC PPP approaches. As the ionospheric observables extracted from the dual-frequency PPP with better accuracy have the identical form with the values from the CCL, the PPP method has been widely applied in the GNSS ionospheric studies [20], [21]. The two methods are based on the hypothesis that the receiver DCB exhibits a high degree of stability over a period of time or within one day. However, this is not the case, and Li *et al.* [22] demonstrated that the receiver DCB variations of the two consecutive hours can reach the 9-ns magnitude. To avoid the effect of the short-term variability of the receiver DCB, the modified CCL (MCCL) method, in which the receiver DCB is estimated when retrieving the ionospheric observables, is developed as the alternative, simple, and effective method [23], [24]. The MCCL is advantageous in which it can avoid the effect of the leveling errors and enables to provide the receiver DCB per epoch as the by-products. Furthermore, Zhang *et al.* [25] proposed the dual-frequency ionosphere-float modified PPP (MPPP) model considering the time-varying receiver DCB to improve the PPP performance.

The aforementioned customary approaches apply the dual-frequency or multifrequency measurements observed from the geodetic-grade receivers to estimate the ionospheric delay based on the ionospheric plasma anisotropy. However, the single-frequency approach is more cost-effective than the multifrequency approach as it can rely only on the mass-market receiver. Zhang *et al.* [26] present the GPS single-frequency ionosphere-float PPP (SFPPP1) method to jointly estimate the ionospheric vertical TEC (VTEC) and satellite DCB. Zhao *et al.* [27] extended the GPS SFPPP1 approach to the multi-GNSS scenarios. Li *et al.* [28] estimated the ionospheric VTEC by the SFPPP1 approach using the BDS-2 B1I data during the low and high sunspot periods. The first contribution of this study is to present a novel single-frequency ionosphere-free-half PPP (SFPPP2) approach to extract the slant ionospheric observables. When the slant ionospheric observables are available, the VTEC can be estimated based on the ionospheric mapping function (MF). The single-layer model (SLM) assumption is widely adopted in the conversion of the slant TEC (STEC) and VTEC for the sake of convenience, in which the VTEC is assumed to be concentrated in the infinitesimal thickness shell at a fixed height [29], [30]. However, the SLM is possible to cause the error of tens of the vertical ranges due to the strong horizontal gradients of the ionospheric ionization [31]. To reduce the error of the MF, the multilayer MF is applied to estimate the VTEC and satellite OSB [32]. This is the second contribution of this work.

In this study, we present a novel SFPPP2 approach to estimate the ionospheric VTEC and satellite pseudorange OSB. The proposed approach applies to all GNSS systems, and we use the BDS as the representative case to validate the method. The SFPPP2 approach is evaluated together with the SFPPP1 and DFPPP1 approaches for comparison. The structure of this study is organized as follows. First, the GNSS general pseudorange and carrier phase observations are introduced. Then, the SFPPP1, SFPPP2, and DFPPP1 approaches are addressed to extract the slant ionospheric observables and estimate the ionospheric VTEC and satellite OSB. After introducing the processing strategies and the experimental data, the performance of the VTEC and BDS satellite OSB estimates is analyzed. Finally, conclusions are given.

II. Methodology

A. Observation Equations

The GNSS undifferenced pseudorange and carrier phase observables of the satellite s for the receiver r on epoch t read [33]

$$\begin{cases} p^s_{r,j}(t) = \rho^s_r(t) + dt_r(t) - dt^s(t) + T^s_r(t) + \mu_j \\ \qquad \cdot I^s_{r,1}(t) + d_{r,j} - d^s_{,j} + \varepsilon^s_{p,j}(t) \\ \phi^s_{r,j}(t) = \rho^s_r(t) + dt_r(t) - dt^s(t) + T^s_r(t) - \mu_j \\ \qquad \cdot I^s_{r,1}(t) + b_{r,j} - b^s_{,j} + N^s_{r,j}(t) + \varepsilon^s_{\phi,j}(t) \end{cases} \tag{1}$$

where $p^s_{r,j}(t)$ and $\phi^s_{r,j}(t)$ denote the pseudorange and carrier phase observations; $\rho^s_r(t)$ denotes the receiver and satellite geometrical range; $dt_r(t)$ and $dt^s(t)$ are the receiver and satellite clock offsets; $T^s_r(t)$ denotes the tropospheric delay due to the neutral atmosphere; $I^s_{r,1}(t)$ denotes the slant ionospheric delay of the first frequency signal; $\mu_j = f_1^2/f_j^2$ denotes the frequency-dependent multiplier factor, where f_j is the jth frequency; $d_{r,j}$ and $d^s_{,j}$ denote the receiver and satellite pseudorange instrumental delays; $b_{r,j}$ and $b^s_{,j}$ denote the carrier phase hardware delays; $N^s_{r,j}(t)$ denotes the integer ambiguity; and $\varepsilon^s_{p,j}(t)$ and $\varepsilon^s_{\phi,j}(t)$ denote the pseudorange and carrier phase measurement noise, including multipath.

B. SFPPP1: Single-Frequency Ionosphere-Float PPP Model

In the SFPPP1 model, the slant ionospheric delay is estimated as the unknown parameter. Generally speaking, when the receiver coordinates are known, we can fix the receiver position to extract the ionospheric delay for better model strength, and thus, there is no estimation of the coordinate increment. Provided that the satellite DCB is unavailable, the

SFPPP1 model for the jth frequency observations reads [34]

$$\begin{bmatrix} \boldsymbol{P}_{\mathrm{SF1},j} \\ \boldsymbol{\Phi}_{\mathrm{SF1},j} \end{bmatrix} = \left[\boldsymbol{e}_2 \otimes \boldsymbol{M}_r, \boldsymbol{e}_{2m}, \mu_j \cdot \boldsymbol{n}_2 \otimes \boldsymbol{I}_m, z_2 \otimes \boldsymbol{I}_m\right] \cdot \boldsymbol{\xi}_{SF1} + \begin{bmatrix} \boldsymbol{\varepsilon}_{\boldsymbol{P}_{\mathrm{SF1},j}} \\ \boldsymbol{\varepsilon}_{\boldsymbol{\Phi}_{\mathrm{SF1},j}} \end{bmatrix}, \boldsymbol{Q}_r \otimes \boldsymbol{Q}_k \quad (2)$$

where $\boldsymbol{P}_{\mathrm{SF1},j} = [p^1_{r,j}(t), \ldots, p^m_{r,j}(t)]^T$ and $\boldsymbol{\Phi}_{\mathrm{SF1},j} = [\phi^1_{r,j}(t), \ldots, \phi^m_{r,j}(t)]^T$ denote the jth frequency observed minus computed (OMC) pseudorange and carrier phase observations vector; $\boldsymbol{e}_m$ denotes the m-row vector where all values are 1; $\boldsymbol{M}_r = [mf^1_{r,j}(t), \ldots, mf^m_{r,j}(t)]^T$ denotes the tropospheric wet MF design matrix with respect to the zenith wet delay (ZWD) ZWD_r; $\boldsymbol{n}_2 = [1, -1]^T$; $z_2 = [0, 1]^T$; $\boldsymbol{I}_m$ denotes the m-dimension identity matrix; $\boldsymbol{\xi}_{\mathrm{SF1}} = [\mathrm{ZWD}_r(t), d\bar{t}_r(t), \boldsymbol{\tau}, \boldsymbol{a}_1]^T$ denotes the estimated parameters of the SFPPP1 model; $d\bar{t}_r(k)$ denotes the estimated receiver clock; $\boldsymbol{\tau} = [\bar{I}^1_{r,1}(t), \ldots, \bar{I}^m_{r,1}(t)]^T$ and $\boldsymbol{a}_1 = [\bar{N}^1_{r,j}(t), \ldots, \bar{N}^m_{r,j}(t)]^T$ denote the estimated ionospheric delay and ambiguity vectors; $\boldsymbol{\varepsilon}_{\boldsymbol{P}_{\mathrm{SF1},j}} = [\varepsilon^1_{p,j}(t), \ldots, \varepsilon^m_{p,j}(t)]^T$ and $\boldsymbol{\varepsilon}_{\boldsymbol{\Phi}_{\mathrm{SF1},j}} = [\varepsilon^1_{\phi,j}(t), \ldots, \varepsilon^m_{\phi,j}(t)]^T$ denote the measurement noise vectors; $\boldsymbol{Q}_r = \mathrm{diag}(\delta^2_p, \delta^2_\phi)$ denotes the zenith direction pseudorange and carrier phase observations precision matrix; $\boldsymbol{Q}_k$ denotes the cofactor matrix with respect to the elevation diversity of m satellites; and $\otimes$ denotes the Kronecker product operation.

Easily understandingly, the raw single-frequency pseudorange and carrier phase equations reveal the problem of rank deficiency. The aforementioned SFPPP1 model is the full-rank model after reparameterization. We re parameterize the estimated receiver clock, ionospheric delay, and ambiguity parameters of the SFPPP1 model as

$$\begin{cases} d\bar{t}_r(t) = dt_r(t) + d_{r,j} - D^1_1 \\ \bar{I}^s_{r,1}(t) = I^s_{r,1}(t) - \mu^{-1}_{\mathrm{GF},12} \cdot d^s_{,\mathrm{GF},12} + D^1_1/\mu_j \\ \bar{N}^s_{r,j}(t) = N^s_{r,j}(t) + b_{r,j} - b^s_{,j} - d_{r,1} \\ \qquad\qquad -\mu_j \cdot \mu^{-1}_{\mathrm{GF},12} \cdot d^s_{,\mathrm{GF},12} + d^s_{,\mathrm{IF},12} + 2D^1_1 \\ D^1_1 = dt_r(1) + d_{r,j} \end{cases} \quad (3)$$

where identifier with $\bar{}$ denotes the reparameterized operation; operation $(\cdot)_{\mathrm{GF},ij} = (\cdot)_i - (\cdot)_j$ denotes the geometry-free (GF) combined operation for the ith and jth frequency signals; and $(\cdot)_{\mathrm{IF},ij} = -\mu^{-1}_{\mathrm{GF},ij}[\mu_j, -\mu_i] \cdot [(\cdot)_i, (\cdot)_j]^T = [\alpha_{ij}, \beta_{ij}] \cdot [(\cdot)_i, (\cdot)_j]^T$ denotes the ionosphere-free combined operation for the ith and jth frequency signals. D^1_1 is introduced here to make the parameter relationship clearer, including the receiver clock with respect to the first epoch $dt_r(1)$.

C. SFPPP2: Single-Frequency Ionosphere-Free-Half PPP Model

The SFPPP2 model is proposed as the novel approach in this study to estimate the ionospheric VTEC and satellite OSB. Transforming the observation equation of the SFPPP1 model with the conversion matrix $(1/2)\boldsymbol{e}^T_2 \otimes \boldsymbol{I}_m$, the SFPPP2 model is established and reads [35], [36]

$$\boldsymbol{P}_{\mathrm{SF2},j} = \left[\boldsymbol{M}_r, \boldsymbol{e}_m, \frac{1}{2}\boldsymbol{I}_m\right] \cdot \boldsymbol{\xi}_{\mathrm{SF2}} + \boldsymbol{\varepsilon}_{\boldsymbol{P}_{\mathrm{SF2},j}}, \frac{1}{4}\boldsymbol{e}^T_2 \cdot \boldsymbol{Q}_r \cdot \boldsymbol{e}_2 \cdot \boldsymbol{Q}_k \quad (4)$$

where $\boldsymbol{P}_{\mathrm{SF2},j} = (\boldsymbol{P}_{\mathrm{SF1},j} + \boldsymbol{\Phi}_{\mathrm{SF1},j}/2)$ and $\boldsymbol{\xi}_{\mathrm{SF2}} = \left[\mathrm{ZWD}_r(t), d\bar{t}_r(t), \boldsymbol{a}_1\right]^T$ denotes the estimated parameters of the SFPPP2 model.

To solve the rank deficiency problem in the SFPPP2 model, the corresponding estimated reparameterized receiver clock and ambiguity parameters read

$$\begin{cases} d\bar{t}_r(t) = dt_r(t) + \frac{1}{2}d_{r,j} + \frac{1}{2}b_{r,j} - D^1_1 \\ \bar{N}^s_{r,j}(t) = N^s_{r,j}(t) - d^s_{,j} - b^s_{,j} + 2d^s_{,\mathrm{IF},12} + 2D^1_1 \\ D^1_1 = dt_r(1) + \frac{1}{2}d_{r,j} + \frac{1}{2}b_{r,j}. \end{cases} \quad (5)$$

As we can see, the SFPPP2 model cannot directly provide the ionospheric observables, and we recover them with the estimated ambiguity parameters. Apart from the estimated ambiguity parameters, the integer ambiguity $N^s_{r,j}(t)$ can also be represented by the pseudorange and carrier phase observation, which reads

$$N^s_{r,j}(t) = \phi^s_{r,j}(t) - p^s_{r,j}(t) + 2\mu_j \cdot I^s_{r,1}(t) + d_{r,j} - d^s_{,j} - b_{r,j} + b^s_{,j}. \quad (6)$$

Substituting $N^s_{r,j}(t)$ into the estimated ambiguity parameter in (5), the ionospheric observables derived by the SFPPP2 model are given as

$$\begin{aligned} &\bar{I}^s_{r,1}(t) \\ &= -\frac{1}{2}\mu^{-1}_j \cdot \left[\phi^s_{r,j}(t) - p^s_{r,j}(t) - \bar{N}^s_{r,j}(t)\right] \\ &= I^s_{r,1}(t) - \mu^{-1}_{\mathrm{GF},12} \cdot d^s_{,\mathrm{GF},12} - \frac{1}{2}\mu^{-1}_j \cdot \left[b_{r,j} - d_{r,j} - 2D^1_1\right]. \end{aligned} \quad (7)$$

As the raw pseudorange observations have larger noise, the carrier phase observations can be utilized to smooth the pseudorange observations in (6). Hence, the Hatch filter is applied and expressed as [37]

$$\begin{cases} p^s_{r,j,\mathrm{sm}}(t) = \omega(t) \cdot p^s_{r,j}(t) \\ \qquad\qquad +[1 - \omega(t)] \cdot p^s_{r,j,\mathrm{prd}}(t), \quad t > 1 \\ p^s_{r,j,\mathrm{prd}}(t) = p^s_{r,j,\mathrm{prd}}(t-1) \\ \qquad\qquad +\left[\phi^s_{r,j}(t) - \phi^s_{r,j}(t-1)\right], \quad t > 1 \\ p^s_{r,j,\mathrm{sm}}(0) = p^s_{r,j}(0) \\ \omega(t) = 1/t, \quad t < M \\ \omega(t) = 1/M, \quad t \geq M \end{cases} \quad (8)$$

where $p^s_{r,j,\mathrm{sm}}(t)$ and $p^s_{r,j,\mathrm{prd}}(t)$ denote the smooth and predicted pseudorange observations. M denotes the smoothing constant and is set as 20 in this study. Although the Hatch filter will introduce the code-carrier divergence in the smoothed pseudorange observation, the effect of the code-carrier divergence is less than the effect of the larger pseudorange noise.

D. DFPPP1: Dual-Frequency Ionosphere-Float PPP Model

When observing the number of m satellites tracking the ith and jth frequency signals by the receiver, the DFPPP1 model

is expressed as [20]

$$\begin{bmatrix} \boldsymbol{P}_{\mathrm{DF1},ij} \\ \boldsymbol{\Phi}_{\mathrm{DF1},ij} \end{bmatrix} = \left[\boldsymbol{e}_4 \otimes \boldsymbol{M}_r, \boldsymbol{e}_{4m}, \boldsymbol{n}_2 \otimes \boldsymbol{\mu}_2 \otimes \boldsymbol{I}_m, \boldsymbol{z}_2 \otimes \boldsymbol{I}_{2m}\right] \cdot \boldsymbol{\xi}_{\mathrm{DF1}} + \begin{bmatrix} \boldsymbol{\varepsilon}_{\boldsymbol{P}_{\mathrm{DF1},ij}} \\ \boldsymbol{\varepsilon}_{\boldsymbol{\Phi}_{\mathrm{DF1},ij}} \end{bmatrix}, \quad \boldsymbol{q_2} \otimes \boldsymbol{Q}_r \otimes \boldsymbol{Q}_m \tag{9}$$

where $\boldsymbol{P}_{\mathrm{DF1},ij} = [p^1_{r,i}(t), p^2_{r,i}(t), \ldots, p^m_{r,j}(t)]^T$; $\boldsymbol{\Phi}_{\mathrm{DF1},ij} = [\phi^1_{r,i}(t), \phi^2_{r,i}(t), \ldots, \phi^m_{r,j}(t)]^T$; $\boldsymbol{\xi}_{\mathrm{DF1}} = [\mathrm{ZWD}_r(t), d\bar{t}_r(t), \boldsymbol{\tau}, \boldsymbol{a}_2]^T$; $\boldsymbol{\mu}_2 = [\mu_i, \mu_j]^T$; $\boldsymbol{a}_2 = [\bar{N}^1_{r,i}(t), \bar{N}^2_{r,i}(t), \ldots, \bar{N}^m_{r,j}(t)]^T$; $\boldsymbol{q}_2 = \mathrm{diag}(q_i^2, q_j^2)$; and q_i denotes the observation noise ratio on the ith frequency.

The corresponding estimated parameters of the DFPPP1 model can be expressed as

$$\begin{cases} d\bar{t}_r(t) = dt_r(t) + d_{r,\mathrm{IF},ij} \\ \bar{I}^s_{r,1}(t) = I^s_{r,1}(t) - \mu^{-1}_{\mathrm{GF},ij} \cdot d^s_{,\mathrm{GF},ij} + \mu^{-1}_{\mathrm{GF},ij} \cdot d_{r,\mathrm{GF},ij} \\ \bar{N}^s_{r,\varsigma}(t) = N^s_{r,\varsigma}(t) + b_{r,\varsigma} - b^s_{,\varsigma} - d_{r,\mathrm{IF},ij} \\ \qquad\qquad + \mu_\varsigma \cdot \mu^{-1}_{\mathrm{GF},ij} \cdot d_{r,\mathrm{GF},ij} \\ \qquad\qquad - \mu_\varsigma \cdot \mu^{-1}_{\mathrm{GF},ij} \cdot d^s_{,\mathrm{GF},ij}, \quad \varsigma = i, j. \end{cases} \tag{10}$$

E. Ionospheric Modeling and Satellite OSB Estimation

The extracted slant ionospheric delays from the SFPPP1, SFPPP2, and DFPPP1 models have unified forms, which reads

$$\begin{aligned} \bar{I}^s_{r,1}(t) &= I^s_{r,1}(t) - \mu^{-1}_{\mathrm{GF},ij} \cdot d^s_{,\mathrm{GF},ij} + \Delta + \varepsilon_I(t) \\ &= \frac{40.28}{f_1^2} \cdot \mathrm{STEC}^s_r(t) - \mu^{-1}_{\mathrm{GF},ij} \cdot d^s_{,\mathrm{GF},ij} + \Delta + \varepsilon_I(t) \end{aligned} \tag{11}$$

with

$$\Delta = \begin{cases} (dt_r(1) + d_{r,j})/\mu_j, & \mathrm{SFPPP1},\ \mathrm{SFPPP2} \\ \mu^{-1}_{\mathrm{GF},ij} \cdot d_{r,\mathrm{GF},ij}, & \mathrm{DFPPP1}. \end{cases} \tag{12}$$

We can see that the ionospheric observables from the SFPPP1 model have the identical form with that from the SFPPP2 model, and the counterpart from the DFPPP1 model is different. In summary, the estimated ionospheric observables can be viewed as the function of the STEC, satellite DCB, and receiver hardware. The ionospheric MF that usually depends on the satellite elevation is the obliquity factor to compute the link of the VTEC and STEC. The single-layer MF is established by assuming that the ionosphere shell is fixed at a certain height. The corresponding obliquity factor of the single-layer MF can refer to the literature [38], [39]. Compared with the single-layer MF, the multilayer MF exhibits the fewer mapping errors, in which the ionosphere structure is divided into numerous thin shells [40]. The method of the multilayer MF can refer to the literature [41].

With the help of ionospheric MF, the STEC can be viewed as the function of the ionospheric VTEC value. To isolate the absolute ionospheric VTEC value, the generalized trigonometric series function (GTSF) is commonly used in the local ionosphere modeling, where the IPP VTEC is modeled as the function of the geographical latitude and time, which can be described as [42]

$$\begin{cases} \mathrm{VTEC}_r(\varphi, T) = \sum_{n=0}^{2}\sum_{m=0}^{2}\left\{E_{nm} \cdot (\varphi - \varphi_0)^n \cdot T^m\right\} \\ \qquad\qquad + \sum_{k=0}^{4}\left\{C_k \cdot \cos(k \cdot T) + S_k \cdot \sin(k \cdot T)\right\} \\ T = \dfrac{2\pi \cdot (t - 14)}{24} \end{cases} \tag{13}$$

where φ and φ_0 denote the IPP and receiver geographical latitudes, respectively.

To isolate the pseudorange OSB values, the satellite DCB in (14) is expressed as the function of the satellite pseudorange OSB. Some specific constraints, including the zero-mean constellation constraint and ionosphere-free combined constraint, are also added in the adjustment solving to solve the rank-deficient system, which can be written as

$$\begin{cases} d^s_{,\mathrm{GF},ij} = d^s_{,i} - d^s_{,j} \\ \sum_{k=0}^{m} d^k_{,i} = 0 \\ \sum_{k=0}^{m} d^k_{,j} = 0 \\ \alpha_{ij} \cdot d^s_{,i} + \beta_{ij} \cdot d^s_{,j} = 0. \end{cases} \tag{14}$$

Hence, the ionospheric observables can be used to estimate the ionospheric VTEC and the satellite pseudorange OSB. Considering the effects of the satellite elevation and local time factors, the ionospheric observable weight in the VTEC modeling can be expressed as [15]

$$p = \frac{1 + \frac{1}{2}\left[\cos\left(\frac{t-2}{12}\pi\right) - 1\right]}{1 + \cos^2 E} \tag{15}$$

where p denotes the ionospheric observable weight.

F. Comparison of PPP Methods

Table I summarizes the differences and similarities of the three PPP methods, including the number of observations and

TABLE I

COMPARISON OF THE TWO SINGLE-FREQUENCY AND ONE DUAL-FREQUENCY PPP MODELS FOR EXTRACTING THE SLANT IONOSPHERIC OBSERVABLES

	SFPPP1	SFPPP2	DFPPP1
Number of observations	2*m*	*m*+*m* (ambiguities)	4*m*
Number of unknown parameters	2*m*+1+sysNum	*m*+1+sysNum+*m* (ambiguities)	3*m*+1+sysNum
Degrees of freedom	-1-sysNum	-1-sysNum	*m*-1-sysNum
Biases in the estimated ionospheric observables	Ionospheric observables, satellite DCB, receiver hardware delay, receiver clock on the first epoch	Ionospheric observables, satellite DCB, receiver hardware delay, receiver clock on the first epoch	Ionospheric observables, satellite DCB, receiver DCB

where 'sysNum' denotes the number of the applied GNSS systems

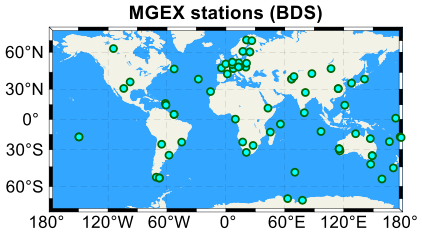

Fig. 1. Distribution of the 77 selected MGEX stations tracking the BDS signals.

unknown parameters, degrees of freedom, and the biases in the estimated ionospheric observables. For the two single-frequency PPP methods, the degrees of freedom are the same. As some of the estimated parameters are linearly dependent, the design matrices of the two models have column rank deficiency. To obtain unique estimated parameters, the corresponding parameters are reparameterized to reconstruct the full rank model. Hence, the number of the unknowns is larger than the number of observations, and thus, the degrees of freedom are negative for the models of the first epoch. For the state of models in the following epoch, the rank deficiencies are eliminated. As the SFPPP2 approach applies the combined observations, the corresponding computational efficiency is higher. For the SFPPP1 and DFPPP1 approaches, the ionospheric terms are directly estimated as unknowns. The difference between the SFPPP1 and SFPPP2 approaches is that the ionospheric observables in the SFPPP2 approach are affected by leveling errors and measurement noises. The difference between the DFPPP1 model and two single-frequency models is that the ionospheric observables constitute the receiver DCB. Theoretically, the ionospheric observables from the dual-frequency PPP model are more accurate than those from the single-frequency PPP approaches.

III. Experimental Results and Analysis

A. Data Processing Strategy

For analyzing the experimental performance, 77 Multi-GNSS Experiment (MGEX) stations that are capable of tracking the BDS (BDS-2 + BDS-3) signals in October 2020 are selected to conduct the SFPPP1, SFPPP2, and DFPPP1 solutions to estimate the ionospheric VTEC and satellite OSB. The corresponding distribution diagram of the MGEX stations is shown in Fig. 1. The BDS-only PPP solutions are selected as the representative schemes of the GNSS systems although the present approaches are also adapted to multi-GNSS scenarios. The single-frequency PPP approaches are based on the BDS-3 B1I signal, and the B1I/B3I dual-frequency measurements are applied for the dual-frequency PPP approach. With respect to the PPP data processing strategy, the Deutsches GeoForschungsZentrum (GFZ) precise orbit and clock products are utilized. The forward and backward Kalman filters are applied, and the ionospheric delay is estimated as the random walk (10^{-4} m^2/s) in SFPPP1 and DFPPP1 solutions. The estimable ionospheric delay absorbs the receiver clock with respect to the first epoch. The satellites with the elevation cutoff of 7.5° are selected for the PPP solutions. In the step of the ionospheric VTEC and satellite OSB estimation, the elevation cutoff of 20° is applied to avoid the effect of the PPP convergence period [43]. The multilayer MF instead of the single-layer MF is applied to alleviate the MF errors. The processing strategies of the other error items can refer to [41].

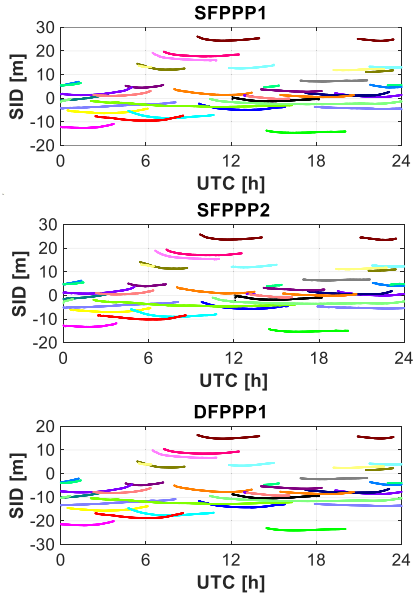

Fig. 2. Estimated slant ionospheric delay at station ULAB on DOY 288, 2020, from the SFPPP1, SFPPP2, and DFPPP1 approaches.

B. Analysis of Slant Ionospheric Observables

We first evaluate the performance of the extracted slant ionospheric observables, which is the prerequisite of the ionospheric VTEC and satellite OSB estimation. The differences of the retrieved ionospheric observables from different approaches can reflect the bias consistency. Suppose that the ionospheric observables from different methods are consistent; their differences should follow the Gaussian distribution. Moreover, as the satellite hardware delay can be eliminated when creating differences for the same satellites, the standard deviation (STD) of the remaining biases can reflect the noise and leveling errors.

Fig. 2 displays the estimated slant ionospheric delays from the two single-frequency PPP models, as well as the DFPPP1 model at one randomly selected station ULAB on day of year (DOY) 288, 2020. The ionospheric observables of the different satellites are represented by different colors. As discussed above, the estimated ionospheric observables from the single-frequency PPP models contain the pure ionospheric values, satellite DCB, receiver hardware, and receiver clock with respect to the first epoch. The ionospheric observables from the dual-frequency PPP include the pure ionospheric values, satellite, and receiver DCB. We can see that the ionospheric observables of the three PPP approaches have a similar variation trend with certain reliability.

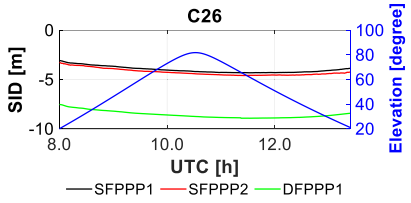

Fig. 3. Slant ionospheric delay estimated from the SFPPP1, SFPPP2, and DFPPP1 solutions against the elevation at C26 at station ULAB on DOY 288, 2020.

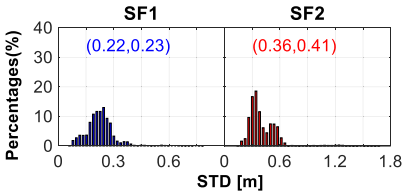

Fig. 4. Histogram distribution of the STD for the slant ionospheric delay difference from the SFPPP1 and SFPPP2 solutions with respect to the DFPPP1 solution. (a) and (b) Corresponding median and mean values.

Putting the estimated ionospheric observables from three PPP approaches together, the ionospheric observables of the three methods against the elevation at C26 at station ULAB on DOY 288, 2020, are depicted in Fig. 3. The ionospheric observables from the dual-frequency PPP model are selected as the reference to indicate the bias consistency. We can see that the reparameterized ionospheric observables from the SFPPP1 and SFPPP2 approaches generally overlap each other, which indicates that the ionospheric observables from two single-frequency PPP solutions are generally consistent with each other. The ionospheric delays from the dual-frequency PPP model are away from that of the single-frequency PPP models for the corresponding ionospheric delays in dual-frequency PPP that encompasses the receiver DCB. As the ionospheric observables from the dual-frequency PPP solution have the highest accuracy, we select the ionospheric observables from the dual-frequency PPP solution as the reference value. We calculated the STD of the daily differences for the ionospheric observables obtained from the SFPPP1 and SFPPP2 approaches with respect to that from the DFPPP1 approach.

Fig. 4 displays the histogram distribution of the STD for the slant ionospheric delay difference from the SFPPP1 and SFPPP2 solutions with respect to the DFPPP1 solution. The median and mean values of the STD are also shown in the figure. The noise and the leveling errors of the ionospheric observables are reflected in the STD of the ionospheric delay difference. The SFPPP1 approach delivers a slightly better agreement than the SFPPP2 solution with respect to the dual-frequency PPP approach. The mean STDs of the ionospheric observable differences for the SFPPP1 and SFPPP2 with respect to the DFPPP1 approach are 0.23 and 0.41 m, respectively. The effects of the pseudorange noises and leveling errors bring about the larger STD in the SFPPP2 approach. Both two single-frequency PPP methods

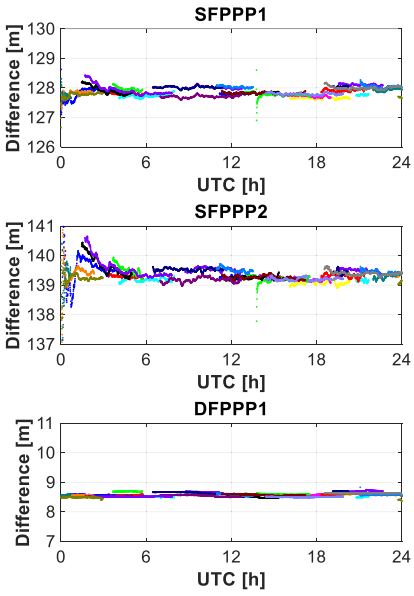

Fig. 5. Single difference of the slant ionospheric observables at the collocated stations WTZS and WTZZ on DOY 288, 2020, for the SFPPP1, SFPPP2, and DFPPP1 solutions.

TABLE II
INFORMATION OF THE SHORT BASELINES

No.	Stations	Baselines	Length	Receiver	Antenna
1	KIT3 KITG	KIT3- KITG	190 m	SEPT ASTERX4 SEPT POLARX5	SEPCHOKE_B3E 6 TRM59800.00
2	RGDG RIO2	RGDG- RIO2	49 m	TRIMBLE ALLOY SEPT ASTERX4	TRM59800.00 SEPCHOKE_B3E 6
3	WTZS WTZZ	WTZS- WTZZ	66 m	SEPT POLARX5TR JAVAD TRE_3 DELTA	LEIAR25.R3 LEIAR25.R3
4	YAR2	YAR2-	2 m	TRIMBLE ALLOY	AOAD/M_T
5	YAR3 YARR	YAR3- YARR	20 m	SEPT POLARX5 SEPT POLARX5	LEIAR25 LEIAT504

are capable of extracting the slant ionospheric observables with the accuracy of submeters.

The single difference of ionospheric observables extracted with the same method at the collocated receivers observing the same satellite will remove the ionospheric effect and corresponding satellite DCB. Hence, we can evaluate the magnitude of the ionospheric observables leveling errors using the measurements from the zero- or short-baseline data. Fig. 5 depicts the single difference of the slant ionospheric observables at the collocated stations WTZS and WTZZ on DOY 288, 2020, for the SFPPP1, SFPPP2, and DFPPP1 solutions. The differences of the observables from different satellites are represented by different colors. The STDs of the single-difference ionospheric observables from the SFPPP1, SFPPP2, and DFPPP1 approaches are 0.14, 0.31, and 0.06 m, respectively. The two single-frequency PPP approaches exhibit the noise level of the submeter, which is considerably larger than that from the DFPPP1 solution with the centimeter noise level.

The five short baselines are established to analyze the leveling errors of the present methods, and the information of the baselines is given in Table II. We processed all the five short baselines, and the average STDs of the ionospheric

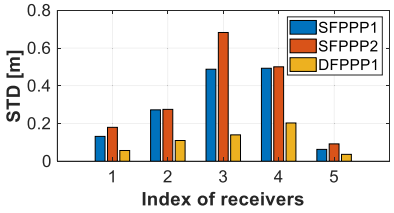

Fig. 6. Average STD of the ionospheric observable differences of the established short baselines for the SFPPP1, SFPPP2, and DFPPP1 approaches.

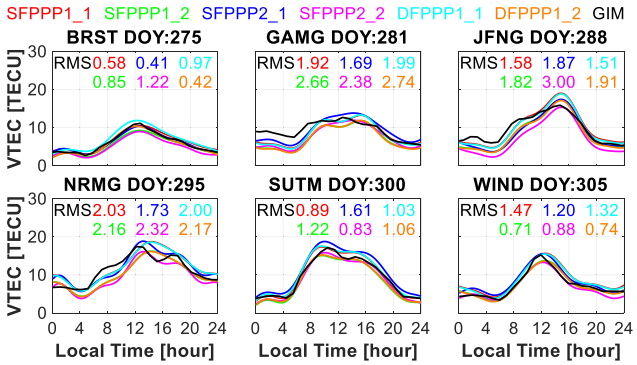

Fig. 7. Time series of the ionospheric VTEC estimates for the random stations BRST, GAMG, JFNG, NRMG, SUTM, and WIND retrieved with the SFPPP1, SFPPP2, and DFPPP1 solutions with the single-layer and multilayer MFs, in which "_1" and "_2" denote the solutions with the single-layer and multilayer MFs and also adopt for Figs. 8–12.

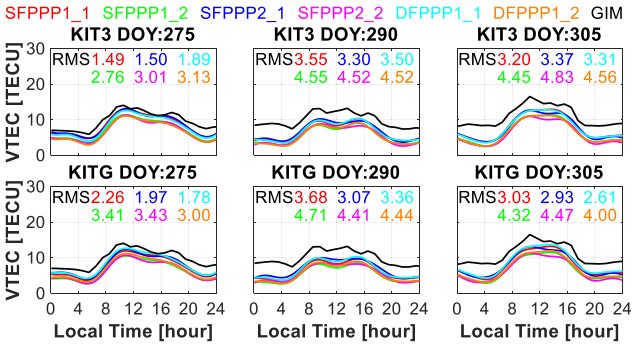

Fig. 8. Time series of the ionospheric VTEC estimates at the collocated stations KIT3 and KITG retrieved with the SFPPP1, SFPPP2, and DFPPP1 solutions with the single-layer and multilayer MFs on DOY 275, 290, and 305, 2020.

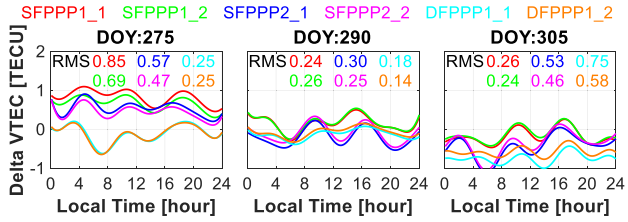

Fig. 9. Time series of the estimated ionospheric VTEC differences at the collocated stations KIT3 and KITG retrieved with the SFPPP1, SFPPP2, and DFPPP1 solutions with the single-layer and multilayer MFs on DOY 275, 290, and 305, 2020.

observable differences of the short baselines for the SFPPP1, SFPPP2, and DFPPP1 approaches are displayed in Fig. 6. The STDs of the ionospheric observable differences from two single-frequency PPP approaches range from 0.1 to 0.7 m. The leveling errors of the SFPPP2 are slightly larger than the SFPPP1 approach. Compared with the single-frequency PPP solution, the leveling errors of the DFPPP1 are evidently reduced with better model strength and more observations.

C. Analysis of Ionospheric VTEC

To evaluate the accuracy and reliability of the proposed approaches, the ionospheric VTEC values are estimated by the SFPPP1, SFPPP2, and DFPPP1 with the single-layer and multilayer MFs, respectively. As the representative case, Fig. 7 depicts the time series of the ionospheric VTEC estimates with the 5-min resolution retrieved with the SFPPP1, SFPPP2, and DFPPP1 solutions at six random stations, BRST, GAMG, JFNG, NRMG, SUTM, and WIND, at one randomly selected day with the single-layer and multilayer MFs. The ionospheric VTEC values from the International GNSS Services (IGS) global ionospheric map (GIM) are also shown in the figure as the reference, which has the accuracy of 2–8 TEC unit (TECU) [44]. We can see that the root mean square (rms) values of the estimated VTEC errors range from 0.4 to 3.0 TECU with respect to the GIM values for the selected stations.

Furthermore, Fig. 8 depicts the time series of the ionospheric VTEC estimates with a 5-min time resolution retrieved with the SFPPP1, SFPPP2, and DFPPP1 approaches with two MFs at a pair of the collocated stations KIT3 and KITG on DOY 275, 290, and 305, 2020, respectively. Theoretically, the VTEC values of the collocated receivers can be considered equally. We can see that the VTEC values of the two stations have a similar diurnal variation, where the minimum values are near the local night and the maximum values are near the local noon. The VTEC values extracted with the single-layer MF have better consistency with the GIM values in which the GIM VTEC values also adopt the single-layer MF, which neglects the ionospheric horizontal gradient [7].

Now, turn to Fig. 9, in which the estimated ionospheric VTEC differences of the two collocated stations KIT3 and KITG retrieved with the SFPPP1, SFPPP2, and DFPPP1 solutions with two MFs on three days are described. The VTEC precision of the corresponding approaches can be reflected by the rms of the ionospheric VTEC single-difference values. The results indicate that the VTEC values derived by the single-frequency PPP approaches are slightly worse than the dual-frequency solution. Moreover, the estimated ionospheric VTEC values by the SFPPP1, SFPPP2, and DFPPP1 approaches with the multilayer MF have better accuracy than that with the single-layer MF.

Fig. 10 depicts the distribution of the rms, mean, and STD of the estimated ionospheric VTEC differences by the SFPPP1, SFPPP2, and DFPPP1 approaches with two MFs with respect to the IGS GIM products. The median and mean values of the rms, mean, and STD are also summarized in the figure. Using the IGS GIM as the reference, the mean rms error of estimated ionospheric VTEC values is approximately 2 TECU.

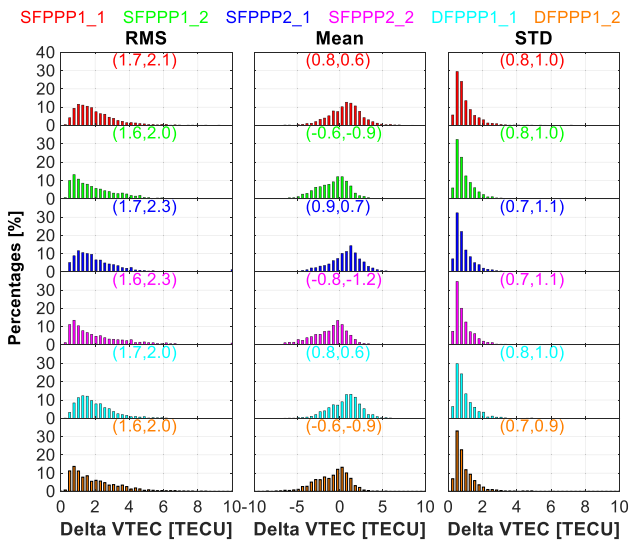

Fig. 10. Distribution of the rms, mean, and STD of the estimated ionospheric VTEC differences by the SFPPP1, SFPPP2, and DFPPP1 approaches with two MFs compared with the IGS GIM products. (a) and (b) Corresponding median and mean values.

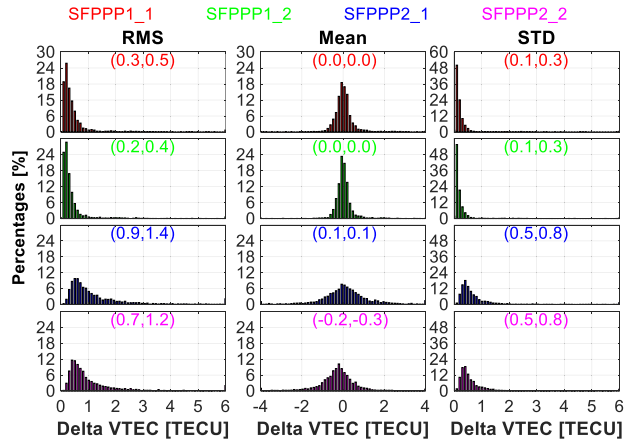

Fig. 11. Distribution of the rms, mean, and STD of the estimated ionospheric VTEC differences compared with the VTEC estimates by the DFPPP method using the corresponding MF.

As a whole, the estimated ionospheric VTEC values with the multilayer MF are less than that from the single-layer MF. No significant differences are observed for the rms and STD of the VTEC differences within the different approaches.

What needs illustration is that the IGS GIM product applies the dual-frequency approach and single-layer MF strategy [45]. To better analyze and quantify the estimated ionospheric VTEC value by the single-frequency PPP approaches, Fig. 11 depicts the rms, mean, and STD of the ionospheric VTEC difference with the two single-frequency PPP approaches with two MFs by comparing the DFPPP1 with the same MF approach. The accuracy of the VTEC estimates with multilayer MF is improved compared with that of the single-layer MF using the values from the dual-frequency PPP as the reference. The ionospheric VTEC accuracy with the SFPPP2 is slightly worse than the SFPPP1 solution.

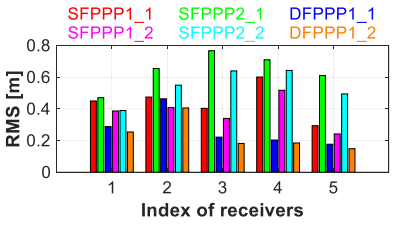

Fig. 12. Average rms of the estimated ionospheric VTEC differences of the established short baselines for the SFPPP1, SFPPP2, and DFPPP1 approaches with the single-layer and multilayer MFs.

The median rms errors of the VTEC estimated by two single-frequency PPP approaches with two MFs are 0.3, 0.2, 0.9, and 0.7 TECU, respectively.

Fig. 12 depicts the average rms of the estimated ionospheric VTEC differences of the five established short baselines for the three PPP methods with the single-layer and multilayer MFs. The ionospheric VTEC accuracy is improved with the multilayer MF compared to the single-layer MF; for instance, the average rms values of the ionospheric VTEC differences for the baseline KIT3-KITG decrease from (0.45, 0.47, 0.29) TECU to (0.39, 0.40, 0.25) TECU for the SFPPP1, SFPPP2, and DFPPP1 approaches, respectively. Due to the effect of the leveling error and pseudorange noises, the ionospheric VTEC accuracy for the SFPPP2 approach is little worse than that from the SFPPP1 approach. The results of the established five short-baseline data indicate that ionospheric VTEC accuracy can reach the submeter level.

D. Analysis of the OSB Estimates

The estimated method of the BDS OSB is similar to the IGGDCB (IGG stands for Institute of Geodesy and Geophysics) [46]. First, we need to precisely extract the slant ionospheric observables based on the full-rank single- or dual-frequency PPP approaches. The next step is to obtain the sums of the satellite and receiver hardware delays for all the stations through station-based ionospheric modeling. After imposing the zero-mean constellation constraint and ionosphere-free combined constraint for all observing satellites, the OSB values on the first and second frequency bands can be determined with high accuracy. In this section, the BDS C2I and C6I OSB estimates are validated with the stability and consistency analysis.

Fig. 13 depicts the overview of the BDS C2I and C6I OSB stability estimated with the SFPPP1, SFPPP2, and DFPPP1 solutions with two MFs in October 2020. It is worth mentioning that the OSB values of different days are transformed to the same zero-mean condition with the specific satellites; otherwise, a systematical shift will arise for all involved satellites. We can see that virtually all estimated satellite OSB are relatively continuous and stable over time. Rarely satellites are discontinued someday, for instance, the C45 satellite shifted several nanoseconds on DOY 288. The OSB time series with different MFs is generally overlapped with each other, and thus, we assumed that the OSB estimation is little affected by the used MF. The OSB time series with three

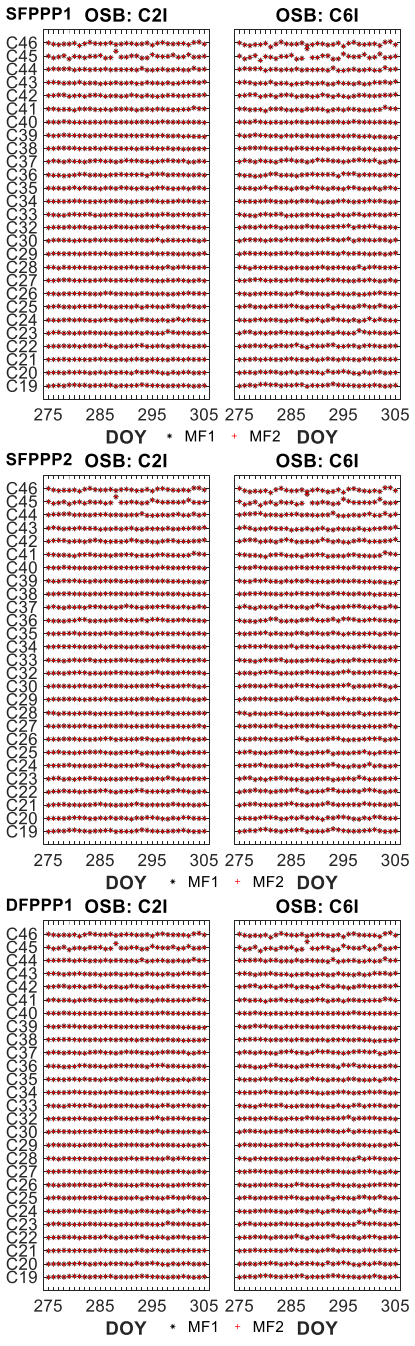

Fig. 13. Time series of the daily BDS-3 C2I and C6I OSB estimates on October 2020 estimated by the SFPPP1, SFPPP2, and DFPPP1 methods. The values are shown with respect to the OSB value of the first day, and the OSB time series is shifted by 10 ns.

approaches has similar variations. The new proposed single-frequency approach is capable of estimating the satellite OSB with certain reliability.

To analyze the estimated OSB stability, Figs. 14 and 15 depict the monthly mean and STD of the BDS C2I and C6I signals with two MFs in October 2020. The BDS OSB values are extensive, in which the mean OSB values range from −90 to 150 ns. In addition to the BDS-2 geostationary orbit (GEO) satellites (C01, C02, C03, C04, and C05), the STDs of the BDS satellites are less than 1 ns. The STDs of the BDS

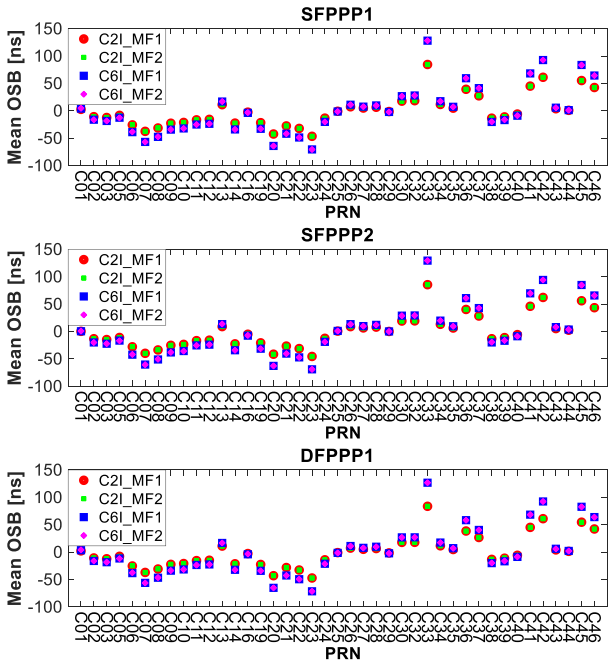

Fig. 14. Mean OSB estimates of the BDS C2I and C6I signals with two MFs on October 2020.

OSB estimated by the SFPPP1 and SFPPP2 approaches are generally consistent with each other. For the DFPPP1 solution, the estimated OSB time series is more stable with a less STD value. Due to the condition of the ionosphere-free combined constraint, the ratio of the mean and STD values of the OSB is fixed with the value of $-\beta_{ij}/\alpha_{ij}$. The OSB stability of the C45 and C46 satellites is worse than that of the other satellites, which is affected by the observation quality.

Fig. 16 depicts the monthly rms of the BDS C2I and C6I OSB estimates with respect to the CAS products. The mean monthly rms of the different constellations, including the GEO, Inclined GeoSynchronous Orbit (IGSO), and medium orbit (MEO), as well as all BDS constellations, is shown in Fig. 16. The consistency of the GEO OSBs is worse than IGSO and MEO with the factor of 2–3. The MEO consistency is slightly worse than the IGSO due to the effect of the C45 and C46 satellites. It is reasonable for the BDS to act as the newly deployed system and part satellites are still in the verification and testing phase. For SFPPP1 solution, rms with respect to CAS product for C2I and C6I with two MFs is (0.38, 0.39, 0.57, 0.59) ns. For SFPPP2 solution, rms with respect to CAS product for C2I and C6I with two MFs is (0.40, 0.41, 0.60, 0.63) ns. For the DFPPP1 solution, rms with respect to CAS product for C2I and C6I with two MFs is (0.34, 0.35, 0.52, 0.54) ns. The proposed SFPPP2 method can provide the BDS OSB estimation with high flexibility and precision.

E. Analysis of the Computation Efficiency

The section analyzes the computation efficiency of the SFPPP1, SFPPP2, and DFPPP1 approaches. The experiment is conducted by the computer with the Windows 10 Operating System and the AMD Ryzen 5 3600 Six-Core Processor with a 3.59-GHz processor. The average computation times

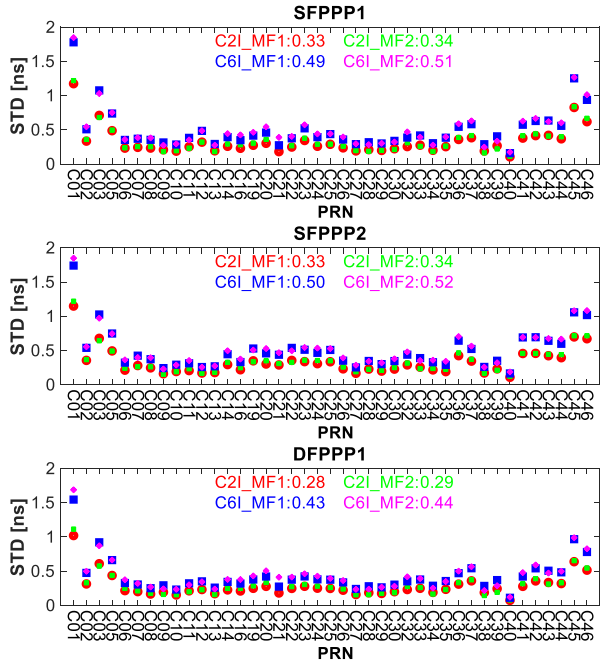

Fig. 15. Monthly STDs of the BDS C2I and C6I OSB estimates with two MFs on October 2020. The mean STDs of the two signals with two MFs are also depicted.

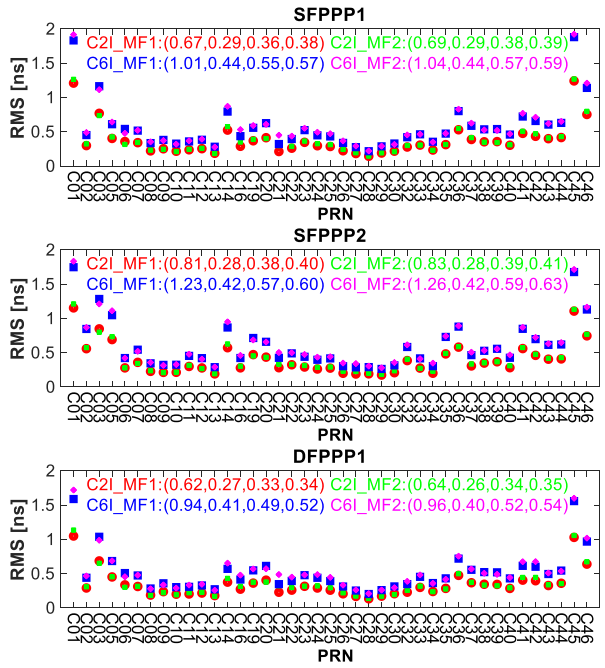

Fig. 16. RMS of the OSB estimates with respect to the CAS OSB products. The mean rms of the two signals with two MFs is also depicted. (a)–(d) Mean rms of the OSB for the GEO, ISGO, MEO, and all satellites.

of the BDS ionospheric VTEC estimation with respect to the SFPPP1, SFPPP2, and DFPPP1 models for the 77 selected stations are 9.9, 7.0, and 12.7 s, respectively. The BDS satellite pseudorange OSB estimation steps can be divided into two steps. The first step computation efficiency is different with the different PPP models. For the second step, the number of satellite and receiver hardware delays from the three models is the same. Hence, the computation time of the second step in the pseudorange OSB estimation is at the same level, whose mean value is 31.7 s. On the premise of the single-thread data processing during the estimation, the computation times of the BDS satellite pseudorange OSB estimation with respect to the SFPPP1, SFPPP2, and DFPPP1 models for the 77 selected stations in one day are 13.2, 9.6, and 16.9 min, respectively. The computation efficiency of the SFPPP2 model is the fastest in which it applies the one ionosphere-free observables. The proposed SFPPP2 model provides an alternative approach with faster computational efficiency for ionospheric VTEC modeling and satellite OSB estimation.

IV. Conclusion

The customary methods to estimate the ionospheric VTEC include the SFPPP1, DFPPP1, and dual-frequency CCL methods with the aid of the ionospheric single-layer MF. The study presented a novel SFPPP2 approach to estimate the ionospheric VTEC and satellite OSB. The satellite OSB parameter is convenient and can be directly corrected in the raw pseudorange observations. The ionospheric multilayer MF is applied to improve the estimated ionospheric VTEC accuracy by considering the effect of the horizontal gradients and vertical ionosphere structures. In this work, we present the SFPPP1, SFPPP2, and DFPPP2 approaches to extract the slant ionospheric observables and estimate the ionospheric VTEC and satellite OSB with the single-layer and multilayer MFs. The performance of the three methods is evaluated in terms of the extracted slant ionospheric observables, estimated ionospheric VTEC, and satellite OSB using the datasets from the 77 MGEX stations in a month. The main conclusions are summarized as follows.

1) The extracted slant ionospheric observables from the SFPPP2 approach are generally consistent with that from the SFPPP1 approach. The pseudorange noises and leveling errors of the extracted ionospheric observables from the SFPPP2 approach are slightly larger than those from the SFPPP1 approach. The single-frequency PPP solutions can extract the slant ionospheric observables with submeter accuracy.
2) The estimated VTEC accuracy from the single-frequency PPP approaches is slightly worse than that from the dual-frequency PPP. With the help of applying ionospheric multilayer MF, the estimated VTEC accuracy is improved. Using the IGS GIM product as the reference, the mean rms error of estimated ionospheric VTEC values is approximately 2 TECU. Using the VTEC values from the dual-frequency PPP with the same MF approach, the accuracy of the estimated VTEC values is less than 1 TECU. With the established five short baselines data, the ionospheric VTEC accuracy can reach the submeter level.
3) The estimated BDS C2I and C6I OSB estimates are analyzed in terms of stability and consistency. The OSB estimated with different MFs is consistent with each other. The satellite OSB time series in a month is continuous and stable with certain reliability. The STDs of the BDS OSB estimated with different approaches are consistent. Using the CAS products as the reference, the accuracy of the GEO OSBs is worse than IGSO and

MEO with the factor of 2–3. For the proposed SFPPP2 solution, rms's with respect to CAS product for C2I and C6I with two MFs are 0.40, 0.41, 0.60, and 0.63 ns.

In summary, the proposed SFPPP2 approach is demonstrated as a reliable and effective method to retrieve the VTEC and satellite pseudorange OSB by mass-market receivers, which is advantageous for only the single-frequency pseudorange and carrier phase measurements.

ACKNOWLEDGMENT

The authors acknowledge that the BeiDou Navigation Satellite System (BDS) observation data were provided by the IGS (ftp://cddis.gsfc.nasa.gov/pub/gps/data/daily/) and the BDS precise orbit and clock products are released by the GFZ (http://www.gfzpotsdam.de/GNSS/products/mgex/).

REFERENCES

[1] S. Jin and K. Su, "PPP models and performances from single- to quad-frequency BDS observations," *Satell. Navigat.*, vol. 1, no. 1, pp. 1–13, Dec. 2020.

[2] Y. Yang, Y. Mao, and B. Sun, "Basic performance and future developments of BeiDou global navigation satellite system," *Satell. Navigat.*, vol. 1, no. 1, pp. 1–8, Dec. 2020.

[3] R. Li *et al.*, "Advances in BeiDou navigation satellite system (BDS) and satellite navigation augmentation technologies," *Satell. Navigat.*, vol. 1, no. 1, pp. 1–23, Dec. 2020.

[4] O. Montenbruck *et al.*, "The multi-GNSS experiment (MGEX) of the international GNSS service (IGS)—Achievements, prospects and challenges," *Adv. Space Res.*, vol. 59, no. 7, pp. 1671–1697, Apr. 2017.

[5] Z. Li *et al.*, "IGS real-time service for global ionospheric total electron content modeling," *J. Geodesy*, vol. 94, no. 3, pp. 1–16, Mar. 2020.

[6] X. Ren, X. Zhang, W. Xie, K. Zhang, Y. Yuan, and X. Li, "Global ionospheric modelling using multi-GNSS: BeiDou, galileo, GLONASS and GPS," *Sci. Rep.*, vol. 6, no. 1, Dec. 2016, Art. no. 33499.

[7] S. Schaer, G. Beutler, M. Rothacher, and T. A. Springer, "Daily global ionosphere maps based on GPS carrier phase data routinely produced by the CODE analysis center," in *Proc. IGS Anal. Center Workshop*, 1996, pp. 1–12.

[8] M. Hernández-Pajares *et al.*, "The ionosphere: Effects, GPS modeling and the benefits for space geodetic techniques," *J. Geodesy*, vol. 85, no. 12, pp. 887–907, 2011.

[9] J. Sanz, J. M. Juan, A. Rovira-Garcia, and G. González-Casado, "GPS differential code biases determination: Methodology and analysis," *GPS Solutions*, vol. 21, no. 4, pp. 1549–1561, Oct. 2017.

[10] O. Montenbruck, A. Hauschild, and P. Steigenberger, "Differential code bias estimation using multi-GNSS observations and global ionosphere maps," in *Proc. Int. Tech. meeting Inst. Navigat.*, Jan. 2014, pp. 802–812.

[11] N. Wang, Y. Yuan, Z. Li, O. Montenbruck, and B. Tan, "Determination of differential code biases with multi-GNSS observations," *J. Geodesy*, vol. 90, no. 3, pp. 209–228, 2016.

[12] *RTCM Standard 10403.3 Differential GNSS (Global Navigation Satellite Systems) Services-Version 3*, RTCM Special Committee, New York, NY, USA, 2016, no. 104.

[13] S. Schaer, "SINEX BIAS—Solution (software/technique) INdependent EXchange format for GNSS BIASes version 1.00," in *Proc. IGS Workshop GNSS Biases*, Bern, Switzerland, 2016, pp. 1–52.

[14] A. Villiger, S. Schaer, R. Dach, L. Prange, A. Sušnik, and A. Jäggi, "Determination of GNSS pseudo-absolute code biases and their long-term combination," *J. Geodesy*, vol. 93, no. 9, pp. 1487–1500, Sep. 2019.

[15] N. Wang, Z. Li, B. Duan, U. Hugentobler, and L. Wang, "GPS and GLONASS observable-specific code bias estimation: Comparison of solutions from the IGS and MGEX networks," *J. Geodesy*, vol. 94, no. 8, pp. 1–15, Aug. 2020.

[16] L. Ciraolo, F. Azpilicueta, C. Brunini, A. Meza, and S. M. Radicella, "Calibration errors on experimental slant total electron content (TEC) determined with GPS," *J. Geodesy*, vol. 81, no. 2, pp. 111–120, 2007.

[17] B. Zhang, J. Ou, Y. Yuan, and Z. Li, "Extraction of line-of-sight ionospheric observables from GPS data using precise point positioning," *Sci. China Earth Sci.*, vol. 55, no. 11, pp. 1919–1928, Nov. 2012.

[18] C. Shi *et al.*, "An enhanced algorithm to estimate BDS satellite's differential code biases," *J. Geodesy*, vol. 90, no. 2, pp. 161–177, Feb. 2016.

[19] L. Chen, W. Yi, W. Song, C. Shi, Y. Lou, and C. Cao, "Evaluation of three ionospheric delay computation methods for ground-based GNSS receivers," *GPS Solutions*, vol. 22, no. 4, p. 125, Oct. 2018.

[20] T. Liu, B. Zhang, Y. Yuan, and M. Li, "Real-time precise point positioning (RTPPP) with raw observations and its application in real-time regional ionospheric VTEC modeling," *J. Geodesy*, vol. 92, no. 11, pp. 1267–1283, Nov. 2018.

[21] B. Zhang, "Three methods to retrieve slant total electron content measurements from ground-based GPS receivers and performance assessment," *Radio Sci.*, vol. 51, no. 7, pp. 972–988, Jul. 2016.

[22] M. Li, Y. Yuan, N. Wang, T. Liu, and Y. Chen, "Estimation and analysis of the short-term variations of multi-GNSS receiver differential code biases using global ionosphere maps," *J. Geodesy*, vol. 92, no. 8, pp. 889–903, Aug. 2018.

[23] B. Zhang, P. J. G. Teunissen, Y. Yuan, X. Zhang, and M. Li, "A modified carrier-to-code leveling method for retrieving ionospheric observables and detecting short-term temporal variability of receiver differential code biases," *J. Geodesy*, vol. 93, no. 1, pp. 19–28, Jan. 2019.

[24] J. Zha, B. Zhang, Y. Yuan, X. Zhang, and M. Li, "Use of modified carrier-to-code leveling to analyze temperature dependence of multi-GNSS receiver DCB and to retrieve ionospheric TEC," *GPS Solutions*, vol. 23, no. 4, pp. 1–12, Oct. 2019.

[25] B. Zhang, C. Zhao, R. Odolinski, and T. Liu, "Functional model modification of precise point positioning considering the time-varying code biases of a receiver," *Satell. Navigat.*, vol. 2, no. 1, pp. 1–10, Dec. 2021.

[26] B. Zhang, P. J. G. Teunissen, Y. Yuan, H. Zhang, and M. Li, "Joint estimation of vertical total electron content (VTEC) and satellite differential code biases (SDCBs) using low-cost receivers," *J. Geodesy*, vol. 92, no. 4, pp. 401–413, 2017.

[27] C. Zhao, Y. Yuan, B. Zhang, and M. Li, "Ionosphere sensing with a low-cost, single-frequency, multi-GNSS receiver," *IEEE Trans. Geosci. Remote Sens.*, vol. 57, no. 2, pp. 881–892, Feb. 2019.

[28] M. Li, B. Zhang, Y. Yuan, and C. Zhao, "Single-frequency precise point positioning (PPP) for retrieving ionospheric TEC from BDS b1 data," *GPS Solutions*, vol. 23, no. 1, p. 18, Jan. 2019.

[29] A. Krankowski, I. I. Shagimuratov, I. I. Ephishov, A. Krypiak-Gregorczyk, and G. Yakimova, "The occurrence of the mid-latitude ionospheric trough in GPS-TEC measurements," *Adv. Space Res.*, vol. 43, no. 11, pp. 1721–1731, Jun. 2009.

[30] M. Hernández-Pajares, D. Roma-Dollase, A. Krankowski, A. García-Rigo, and R. Orús-Pérez, "Methodology and consistency of slant and vertical assessments for ionospheric electron content models," *J. Geodesy*, vol. 91, no. 12, pp. 1405–1414, Dec. 2017.

[31] A. Komjathy, L. Sparks, A. J. Mannucci, and A. Coster, "The ionospheric impact of the October 2003 storm event on wide area augmentation system," *GPS Solutions*, vol. 9, no. 1, pp. 41–50, Apr. 2005.

[32] M. M. Hoque, N. Jakowski, and J. Berdermann, "A new approach for mitigating ionospheric mapping function errors," in *Proc. ION GNSS*, Tampa, FL, USA, Sep. 2014.

[33] A. Leick, L. Rapoport, and D. Tatarnikov, *GPS Satellite Surveying*. Hoboken, NJ, USA: Wiley, 2015.

[34] O. Sterle, B. Stopar, and P. P. Prešeren, "Single-frequency precise point positioning: An analytical approach," *J. Geodesy*, vol. 89, no. 8, pp. 793–810, Aug. 2015.

[35] T. P. Yunck, "Coping with the atmosphere and ionosphere in precise satellite and ground positioning," *Environ. Effects Spacecraft Positioning Trajectories*, vol. 73, pp. 1–16, Jan. 1993.

[36] B. Li, N. Zang, H. Ge, and Y. Shen, "Single-frequency PPP models: Analytical and numerical comparison," *J. Geodesy*, vol. 93, no. 12, pp. 2499–2514, Dec. 2019.

[37] H. K. Lee and C. Rizos, "Position-domain Hatch filter for kinematic differential GPS/GNSS," *IEEE Trans. Aerosp. Electron. Syst.*, vol. 44, no. 1, pp. 30–40, Jan. 2008.

[38] H. Jiang, Z. Wang, J. An, J. Liu, N. Wang, and H. Li, "Influence of spatial gradients on ionospheric mapping using thin layer models," *GPS Solutions*, vol. 22, no. 1, pp. 1–14, Jan. 2018.

[39] C. Brunini and F. Azpilicueta, "GPS slant total electron content accuracy using the single layer model under different geomagnetic regions and ionospheric conditions," *J. Geodesy*, vol. 84, no. 5, pp. 293–304, 2010.

[40] M. M. Hoque and N. Jakowski, "Mitigation of ionospheric mapping function error," in *Proc. ION GNSS*. Nashville, TN, USA: Inst. Navigat., Sep. 2013, pp. 1848–1855.

[41] K. Su, S. Jin, J. Jiang, M. Hoque, and L. Yuan, "Ionospheric VTEC and satellite DCB estimated from single-frequency BDS observations with multi-layer mapping function," *GPS Solutions*, vol. 25, no. 2, pp. 1–17, Apr. 2021.

[42] Y. Yuan and J. Ou, "A generalized trigonometric series function model for determining ionospheric delay," *Prog. Natural Sci.*, vol. 14, no. 11, pp. 1010–1014, Nov. 2004.

[43] Y. Xiang, Y. Gao, J. Shi, and C. Xu, "Consistency and analysis of ionospheric observables obtained from three precise point positioning models," *J. Geodesy*, vol. 93, no. 8, pp. 1161–1170, Aug. 2019.

[44] M. Hernàndez-Pajares *et al.*, "The IGS VTEC maps: A reliable source of ionospheric information since 1998," *J. Geodesy*, vol. 83, no. 3, pp. 263–275, Mar. 2009.

[45] G. Jee, H.-B. Lee, Y. H. Kim, J.-K. Chung, and J. Cho, "Assessment of GPS global ionosphere maps (GIM) by comparison between CODE GIM and TOPEX/Jason TEC data: Ionospheric perspective," *J. Geophys. Res., Space Phys.*, vol. 115, no. A10, Oct. 2010, Art. no. A10319.

[46] Z. Li, Y. Yuan, H. Li, J. Ou, and X. Huo, "Two-step method for the determination of the differential code biases of COMPASS satellites," *J. Geodesy*, vol. 86, no. 11, pp. 1059–1076, 2012.

Ke Su was born in Jiangsu, China, in November 1994. He is currently pursuing the Ph.D. degree with the Shanghai Astronomical Observatory, Chinese Academy of Sciences, Shanghai, China.

His research interests include the Global Navigation Satellite System (GNSS) ionosphere and precise point positioning (PPP) applications.

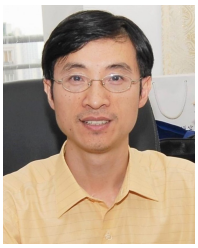

Shuanggen Jin (Senior Member, IEEE) was born in Anhui, China, in September 1974. He received the B.Sc. degree in geodesy from Wuhan University, Wuhan, China, in 1999, and the Ph.D. degree in geodesy from the University of Chinese Academy of Sciences, Beijing, China, in 2003.

He is currently a Professor with the Shanghai Astronomical Observatory, Chinese Academy of Sciences (CAS), Shanghai, China, and a Professor and the Dean of the Nanjing University of Information Science and Technology, Nanjing, China. He has authored/coauthored over 500 papers in peer-reviewed journals and proceedings, ten patents/software copyrights, and ten books/monographs with more than 8000 citations and H-index > 45. His research areas include satellite navigation, remote sensing, and space/planetary geodesy.

Prof. Jin is also a fellow of the International Association of Geodesy (IAG) and the International Union of Geodesy and Geophysics (IUGG) and a member of the Turkish Academy of Sciences, the Russian Academy of Natural Sciences, the European Academy of Sciences, and the Academia Europaea. He received one first-class and four second-class prizes of provincial awards, the 100-Talent Program of CAS, and the Leading Talent of Shanghai. He is the Chair of the IUGG Union Commission on Planetary Sciences (UCPS) (2015–2023). He was the President of the International Association of Planetary Sciences (IAPS) from 2015 to 2019 and the International Association of Chinese Professionals in Global Positioning Systems (CPGPS) from 2016 to 2017 and the Vice-President of the IAG Commission from 2015 to 2019. He has been the Editor-in-Chief of *International Journal of Geosciences*, an Editor of *Geoscience Letters*, an Associate Editor of IEEE TRANSACTIONS ON GEOSCIENCE AND REMOTE SENSING and *Journal of Navigation*, and an Editorial Board Member of *Sensors, Remote Sensing*, *GPS Solutions*, and *Journal of Geodynamics*.